




RESEARCH ARTICLE | FEBRUARY 02 2023

Cavitation bubble dynamics and microjet atomization near tissue-mimicking materials

Special Collection: [Cavitation](#)

A. B. Sieber ; D. B. Preso ; M. Farhat 

 Check for updates

Physics of Fluids 35, 027101 (2023)

<https://doi.org/10.1063/5.0136577>



View
Online



Export
Citation

[CrossMark](#)

Articles You May Be Interested In

Features of the laminar-turbulent transition in supersonic axisymmetric microjets

AIP Conference Proceedings (October 2016)

Microjetting from wave focusing on oscillating drops

Physics of Fluids (May 2007)

Microjetting from a grooved Al surface under supported and unsupported shocks

Journal of Applied Physics (August 2014)

Cavitation bubble dynamics and microjet atomization near tissue-mimicking materials

Cite as: Phys. Fluids **35**, 027101 (2023); doi: [10.1063/5.0136577](https://doi.org/10.1063/5.0136577)

Submitted: 27 November 2022 · Accepted: 15 January 2023 ·

Published Online: 2 February 2023



View Online



Export Citation



CrossMark

A. B. Sieber,^{a)}  D. B. Preso,^{b)}  and M. Farhat 

AFFILIATIONS

Institute of Mechanical Engineering, École Polytechnique Fédérale de Lausanne, Avenue de Cour 33 Bis, 1007 Lausanne, Switzerland

Note: This paper is part of the special topic, Cavitation.

^{a)} Author to whom correspondence should be addressed: armand.sieber@epfl.ch

^{b)} Electronic mail: davide.preso@epfl.ch

ABSTRACT

In recent years, considerable interest has been devoted to the interactions between cavitation bubbles and tissue-mimicking materials due to their promising applications in medicine and biomedical sciences. The strong fluid–structure interaction between a cavitation bubble and these elastic surfaces triggers unique collapse dynamics, characterized by bubble splitting and subsequent microjetting phenomena that can damage adjacent boundaries. In this work, we investigate how the elasticity of the boundary and the distance between the bubble and the elastic surface affect the bubble dynamics and the velocity of its microjet. To this end, we generate single laser-induced cavitation bubbles in the vicinity of agarose hydrogels with different degrees of elasticity and follow the bubble dynamics using high-speed imaging techniques, with a special focus on the formation and evolution of the microjets. We provide a time-resolved evidence of the atomization of the liquid microjet within the bubble, which precedes the establishment of a fully liquid microjet. The atomized portion of the microjet can reach supersonic velocities of up to 2000 ms^{-1} , while the ensuing fully developed liquid microjet travels at averaged speeds of up to 1000 ms^{-1} . To gain further insight into the bubble dynamics leading to the formation of these very fast microjets, we also propose a numerical model based on the boundary integral method and observe a remarkable agreement between the numerical simulations and the experimental observations.

© 2023 Author(s). All article content, except where otherwise noted, is licensed under a Creative Commons Attribution (CC BY) license (<http://creativecommons.org/licenses/by/4.0/>). <https://doi.org/10.1063/5.0136577>

I. INTRODUCTION

The interactions of cavitation bubbles with elastic interfaces have attracted an increasing interest in recent decades. This interest is mainly driven by the numerous applications of cavitation bubbles in modern medical procedures, where the bubble interact with compliant tissue layers. For example, cavitation bubbles are used for targeted drug delivery,^{1–3} ultrasound-based tissue ablation,^{4–6} or as a contrast agent in ultrasound imaging.^{7–9} On the other hand, they are also associated with certain laser-based medical procedures.^{10–12} Depending on the medical application, the reported bubbles can reach sizes ranging from a few micrometers² to several millimeters.¹¹

Given the nature of these applications, understanding the detailed bubble dynamics and its ability to damage and penetrate the adjacent tissue layers is essential to optimize the procedure efficiency and minimize unwanted tissue injury. To assess these dynamics, experimental studies on the interactions of cavitation bubbles with biological tissue are often reduced to the growth and collapse of a single initially

spherical bubble in the vicinity of a tissue-mimicking material (TMM) or an elastic membrane. Kodama and Tomita¹³ conducted one of the first experiments on the dynamics of cavitation bubbles near a TMM. Their study focused on the dynamics of a single cavitation bubble near a gelatin surface and the interaction of a gas bubble attached to the gelatin surface with a shock wave. The authors observed that the cavitation bubble tended to move away from the elastic boundary but found that a liquid microjet formed inside the acoustically driven gas bubble and penetrated the gelatin. Concurrently, Brujan *et al.*^{14,15} conducted a thorough study of the interaction of laser-induced cavitation bubbles with polyacrylamide hydrogels (PAA) of different elasticity. They observed complex bubble dynamics characterized by bubble splitting into two parts and its centroid either migrating toward or away from the elastic boundary. The authors also emphasized the strong dependence of the bubble behavior on the distance to the interface and on the elasticity of the boundary, especially with respect to the velocity and orientation of the microjet and the direction of bubble migration.

They moreover concluded that the penetration of the fluid jet into the boundary was one of the main mechanisms responsible for cavitation-induced tissue ablation. Other studies examined the effects of rubber¹⁶ and silicon gel^{17,18} boundaries on the bubble dynamics. Shaw *et al.*¹⁹ and Orthaber *et al.*²⁰ studied the interactions of cavitation bubbles with a thin elastic membrane. Their study showed similar bubble dynamics than the ones near thick TMM. Orthaber *et al.*²⁰ moreover reported a perforation of the membrane that was attributed to the bubble's microjet. In other works, the effects of fluid viscosity were also explored,²¹ and it was found that the microjet velocity decreased with increasing viscosity, whilst a study on the effects of different fluids on each side of the membrane revealed significant differences in bubble behavior.²² In parallel to the experimental works mentioned above, numerical studies have also been carried out on the interaction of a single cavitation bubble with an elastic interface. Among the various numerical methods available, the boundary integral method (BIM) has been found to be particularly suitable for this application.^{23–28} In these simulations, the biological tissue is generally modeled as a second fluid, with elastic effects accounted for by changing the dynamic conditions at the boundary between the two fluids. The numerical results thus obtained show good qualitative agreement with the experiments and capture the main features of the bubble dynamics near elastic boundaries.

The current state of research seemingly advocates the bubble microjet as the main cause of damage and perforation of TMMs. However, there are still open questions about the actual dynamics of this microjet. For example, little is known about the bubble dynamics that immediately precede the formation of the microjet and how the microjet evolves within the bubble after its inception. Such an analysis would provide clearer insight into the underlying mechanisms that are ultimately responsible for TMM damage. In this work, we therefore study the dynamics of millimeter-sized laser-induced cavitation bubbles near agarose hydrogels, which are natural polymers often used as tissue phantoms. Their mechanical properties can be easily tuned by changing the agarose concentration to mimic different tissue types. We vary the Young's modulus of the hydrogels between ~ 70 and ~ 690 kPa, which covers, for example, the mechanical properties of human tissues such as cardiac muscle cells [~ 100 kPa (Ref. 29)], corneas [~ 290 kPa (Ref. 30)], or gastrointestinal tissues [~ 320 – 790 kPa (Ref. 31)]. We study the dynamics of cavitation bubbles at different distances from the various hydrogels, with a particular focus on the initiation and evolution of the microjets. In addition, we propose a boundary integral method (BIM) model to gain further insight into the bubble dynamics leading to the formation of these microjets.

The present work is organized as follows. In Sec. II, the preparation of the agarose hydrogels and their mechanical testing are described. Then, the experimental setup for cavitation bubble generation and the BIM model are introduced. The results are presented in Sec. III, where we give an overview of the bubble dynamics near different hydrogels and a dedicated description of the associated microjets. We discuss the results in Sec. IV and conclude this work in Sec. V.

II. MATERIALS AND METHODS

A. Agarose hydrogels

Agarose hydrogels are prepared in batches with an agarose concentration, c , of 1%, 2%, 3%, and 4% in weight (w/w). To achieve the desired concentrations, a weighed amount of agarose powder (Fisher

Bioreagents, Molecular Biology Grade) is added to a volumetric flask containing de-ionized water. The flask is then placed in a bain-marie at $\sim 99^\circ\text{C}$, and its content is continuously stirred until the agarose powder is completely dissolved. In addition to dissolution, this process also allows a good degassing of the solution so that no bubbles are trapped in the hydrogel during the final polymerization phase. Although the flask is corked when immersed in the bain-marie, some vapor is allowed to escape to equalize the internal pressure of the flask. The flask is therefore carefully weighed before and after the bath, and finally water at $\sim 99^\circ\text{C}$ is added to the solution to balance the evaporated loss and maintain the desired solute–solvent ratio. We then cast the solution into cylindrical molds (radius = 3.5 cm, height = 1.3 cm), which are preheated in oven to $\sim 70^\circ\text{C}$ to avoid a thermal shock with the solutions. The radius of the hydrogel molds, approximately nine times larger than the maximum radius of the bubbles, has been chosen following various tests to ensure that border effects do not impact the bubble dynamics. We also note that the maximum downward deformation of the hydrogel resulting from bubble oscillation is less than 10% of the mold height, which ensures that there is no border effect in this direction either. During the solidification phase, the molds are covered to minimize water losses due to evaporation and left at room temperature until the hydrogel has formed. They are then removed from the molds, immersed in de-ionized water, and stored in a refrigerator at $\sim 4^\circ\text{C}$. The hydrogels are used for experiments within one day of their preparation to avoid degradation.

The elastic properties of the agarose hydrogels are determined by uniaxial compression tests carried out at room temperature with a ZwickRoell Z005 universal testing machine (ZwickRoell GmbH & Co. KG, Ulm, Germany). Cylindrical hydrogel specimen (cast in molds 8 mm diameter \times 8 mm length) are sandwiched between two compression platens, and a constant strain rate of $1\% \text{ s}^{-1}$ is applied. The strain rate was chosen to avoid permeation of water through the porous hydrogel, which has been reported to occur at strain rates of less than $0.7\% \text{ s}^{-1}$ for samples of similar size. This ensures that the hydrogels adopt an incompressible behavior in the linear strain–stress regime. This regime is characterized by a Poisson's ratio $\nu \approx 0.5$. The strain–stress curve gives the Young's modulus, E , of the specimen, which is evaluated between 0% and 5% strain and averaged over five separate compression tests. The results are shown in the Fig. 1 along the compression Young's modulus measured in other studies.^{32–34} We moreover provide a power-law scaling to relate the Young's modulus to the agarose concentration

$$E = 69.9c^{1.6} \text{ kPa}, \quad (1)$$

where c is in % (w/w).

B. Laser-induced cavitation bubble

Single cavitation bubbles are generated by focusing a frequency-doubled Q-switched Nd:YAG pulsed laser in a $18 \times 18 \times 19 \text{ cm}^3$ transparent test chamber, filled with de-ionized water. The 9 ns and 532 nm laser pulse is first expanded to a diameter of 43 mm by a custom-made Galilean beam expander. It is then focused into water using an immersed aluminum off-axis parabolic mirror with a high convergence angle (45°) to generate a plasma from which the bubble explosively emerges. The use of a parabolic mirror creates a nearly point-like plasma, thus yielding bubbles with high initial sphericity.

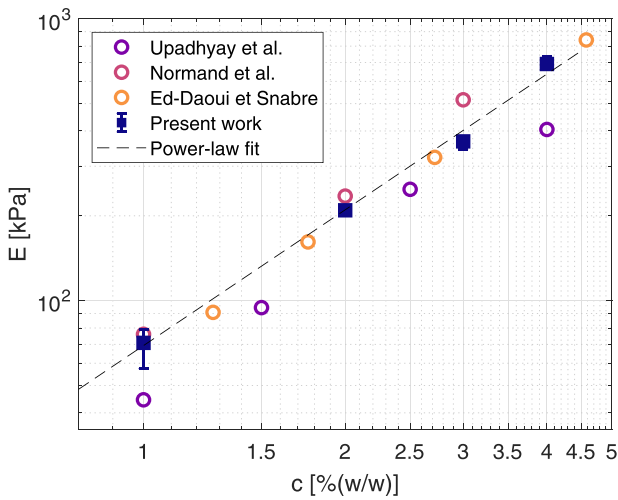


FIG. 1. Young's modulus determined by compression tests as a function of the agarose concentration in the hydrogels. Indigo square refers to the present work, where the error bar displays the range of the data measured, purple circle are from Upadhyay *et al.*,³³ pink circle are from Normand *et al.*,³² and orange circle are from Ed-Daoui and Snabre.³⁴ The dashed line is the power-law fit provided in Eq. (1) of our experimental data.

The dynamics of the bubble is recorded with the Shimadzu HPV-X2 high-speed camera using framing rates between $200\,000$ and 10×10^6 frames s^{-1} . The bubble is either illuminated by back-lighting with a collimated LED light beam to perform shadowgraphs, or through a high-intensity flashlamp to visualize the bubble interior. A detailed description of the experimental setup can be found elsewhere.³⁵

Bubbles with a maximum radius $R_{max} \approx 3.7$ mm are generated at defined distances above the agarose hydrogels. To characterize the proximity of the bubble to the boundary, we use the stand-off parameter, $\gamma = s/R_{max}$, where s is the distance between the initial bubble center and the gel. The distance s is adjusted using a linear translation stage acting on the position of the hydrogel, while the bubble maximum radius is taken as the maximum radius the bubble would attain in an unbounded liquid.^{35–37} We study stand-off distances ranging between $\gamma \approx 0.3$ and 1.5 . We did not investigate smaller stand-off distances as to avoid burning the agarose hydrogels with the initiation plasma nor did we report larger stand-off distances as the bubble-boundary interactions are weak.

C. BIM

Klaseboer and Khoo²⁴ proposed one of the first implementations of an axisymmetric BIM for simulating the dynamics of cavitation bubbles near elastic boundaries. The elastic material was modeled as a second fluid, and elastic effects were accounted for by changing the dynamic conditions at the fluid–fluid interface. This was accomplished by relating the pressure directly above and directly below the fluid interface through an additional pressure term that scales proportionally to the displacement of the interface. Although the authors reported good qualitative agreement with experimental observations of bubble dynamics near PAA hydrogels, we note that the bubble behavior studied in this work cannot be accurately predicted by this

model without tailoring it to our needs. We therefore propose a modified numerical model based on the work of Klaseboer and Khoo,²⁴ where we change the dynamic conditions at the fluid–fluid interface. The bubble evolves in water, with density ρ_w and far-field pressure p_0 . The agarose hydrogel is modeled as a second fluid, with density ρ_a . Both fluids share an infinite, initially flat, interface whose motion is governed by the bubble dynamics. The fluids are considered inviscid, incompressible, and irrotational. Consequently, the Laplace's equation is valid in both fluids and the associated velocity fields are related to the velocity potentials, $\phi_{w,a}$, as $\mathbf{u}_{w,a} = \nabla \phi_{w,a}$. At the fluid–fluid interface, the normal velocities are continuous, $\partial \phi_w / \partial n = -\partial \phi_a / \partial n$, where the minus sign appears because the normal vectors on each side of the interface point in opposite directions. We model the elastic properties of the hydrogel by considering an interfacial tension between the two immiscible fluids. Thus, the pressure directly above and directly below the interface can be related by the Young–Laplace equation. This equation provides the normal stress balance at the fluid–fluid interface with $p_w = p_a + \sigma(K_1 + K_2)$, where σ is the interfacial tension, K_1 and K_2 are the principal curvatures of the interface, and p_w and p_a are the local pressures in the water and agarose hydrogel, respectively. With this approach, we model the agarose hydrogels in a similar way to other authors^{25,27} who have studied the dynamics of cavitation bubbles near elastic membranes. The effect of interfacial tension on the behavior of the interface can be interpreted as follows. The fluid–fluid interface is in equilibrium when flat, but its surface area increases when it deforms, so does its potential energy as $U_\sigma = \sigma \Delta A$, where ΔA represents the additional surface area. The surface tension will thus work to return the interface to its original equilibrium position. The larger the value of σ , the less the interface can deviate from its rest position. When $\sigma = 0$, the pressure on both sides of the interface is continuous regardless of the deformation. The interfacial tension thus acts analogously to a spring that is subjected to a displacement. A schematic of the numerical domain is provided in Fig. 2.

We consider a bubble with constant vapor pressure inside, p_v , such that the dimensionless time evolution of the potential on its surface is given by the Bernoulli equation^{35,38,39}

$$\frac{D\phi_w}{Dt} = \frac{|\mathbf{u}_w|^2}{2} + 1, \tag{2}$$

where the lengths are scaled by the unbounded bubble maximum radius R_{max} , and the time is scaled by $R_{max} / \sqrt{(p_0 - p_v) / \rho_w}$.

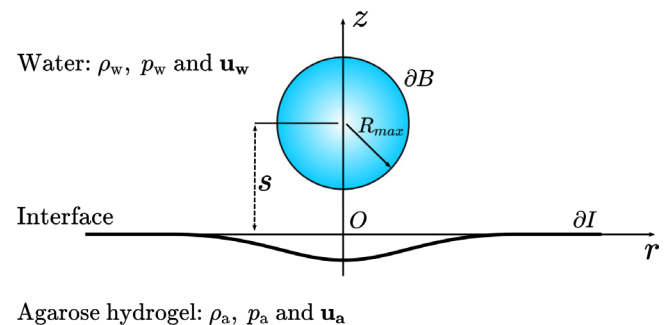


FIG. 2. Schematic of the numerical domain.

Following a derivation introduced by Klaseboer and Khoo,^{23,24} the dimensionless equation for the time evolution of the potential on the fluid–fluid interface is given by

$$\frac{D}{Dt}(\phi_a - \alpha\phi_w) = \left(\mathbf{u}_w \cdot \mathbf{u}_a - \frac{|\mathbf{u}_a|^2}{2} - \alpha \frac{|\mathbf{u}_w|^2}{2} \right) + \alpha \bar{\sigma} \bar{K}, \quad (3)$$

where $\alpha = \rho_w/\rho_a$ is the ratio of the densities of the two fluids, $\bar{\sigma} = \sigma/[R_{\max}(p_0 - p_v)]$ is the dimensionless tension across the interface, and \bar{K} is the dimensionless surface curvature. Given that Laplace’s equation is satisfied in the two fluids, the normal components of the velocity potentials are derived using the BIM formulation. For the water, the domain is delimited by the boundary ∂D_w that consists of the surface of the bubble ∂B , and the fluid–fluid interface ∂I . For the agarose, the domain is solely bounded by the fluid–fluid interface ∂I . The following boundary integral equations can thus be derived:

$$c_{p,w}(\mathbf{y})\phi_w(\mathbf{y}) + \int_{\mathbf{x} \in \partial D_w} \phi_w(\mathbf{x}) \frac{\partial G(\mathbf{y}, \mathbf{x})}{\partial n} ds = \int_{\mathbf{x} \in \partial D_w} G(\mathbf{y}, \mathbf{x}) \frac{\partial \phi_w(\mathbf{x})}{\partial n}, \quad (4)$$

$$c_{p,a}(\mathbf{y})\phi_a(\mathbf{y}) - \int_{\mathbf{x} \in \partial I} \phi_a(\mathbf{x}) \frac{\partial G(\mathbf{y}, \mathbf{x})}{\partial n} ds = \int_{\mathbf{x} \in \partial I} G(\mathbf{y}, \mathbf{x}) \frac{\partial \phi_a(\mathbf{x})}{\partial n}, \quad (5)$$

where $G(\mathbf{y}, \mathbf{x}) = 1/|\mathbf{y} - \mathbf{x}|$ is the Green function, \mathbf{y} is a point in the domain, and $c_{p,w}$ and $c_{p,a}$ are the solid angles. The two solid angles satisfy $c_{p,w} + c_{p,a} = 4\pi$ at the interface.^{23–25} Since the potentials $\phi_{w,a}$ are known at the interfaces ∂B and ∂I , the tangential velocity is also known along the boundaries, and the kinematic condition $D\mathbf{x}/Dt = \nabla\phi_w$ is used to update the position of all surfaces. At the beginning of the simulation, the bubble is taken as a sphere of radius $R_0 = 0.1R_{\max}$. The associated initial time t_0 corresponds to the time it takes a Rayleigh bubble to grow from inception to R_0 , and the potential, $\phi_{b,0}$, is derived from the Rayleigh solution at t_0 , as suggested by Blake *et al.*³⁸ The fluid–fluid interface is initially flat, with $\phi_{w,b,0} = 0$. The model computes the bubble dynamics as long as its surface is single-connected, which we believe to be sufficient in the context of this work.

It remains to define the mechanical properties of the agarose gel, namely, the density ρ_a and the surface tension σ . The density of the hydrogel is defined as $\rho_a = (c\rho_s + (100 - c)\rho_w)/100$, with ρ_s the

agarose powder density. We take $\rho_s \approx 1.65 \text{ g/cm}^3$ as measured by pycnometry by Ed-Daoui and Snabre³⁴ for agarose powder. The definition of σ is more complex, and we propose an argument based on an energetic consideration to relate its value to the actual elastic properties of the agarose hydrogel, i.e., the Young’s modulus. The rationale and derivations for this consideration are detailed in Appendix A. It results that the dimensionless surface tension is expressed as follows:

$$\bar{\sigma} = \frac{4}{3\pi} \frac{E}{(1 - \nu^2)\Delta p}, \quad (6)$$

where the Young’s modulus E is set as $E = 69.9c^{1.6}$ kPa, as found and derived in Sec. II A, the Poisson’s ratio is assumed to be $\nu = 0.5$ and $\Delta p = p_0 - p_v$.

III. RESULTS

The dynamics of a cavitation bubble near an agarose hydrogel differ substantially from that of a similar bubble near a rigid surface, as highlighted in Fig. 3. Figure 3(a) shows the shape of the bubble in the final instants of its collapse ($0.2 \mu\text{s}$ before the onset of its microjet) near the 2% (w/w) agarose hydrogel for different values of γ . Its shape is systematically compared to the one of a similar bubble developing near a rigid boundary at an identical time. While a bubble near a rigid boundary assumes a hemispherical shape when γ is reduced, a bubble near the elastic boundary transitions from a pear-shaped form to a conical shape. Based on this consideration, we identify two oscillatory regimes associated with two ranges of standoff distances. At $\gamma \geq 0.8$, the bubble remains at a considerable distance from the interface in the final moments of its collapse, retaining the shape of a pear. The ensuing microjet, directed toward the elastic boundary, travels through water before impinging on the boundary. On the other hand, if the bubble develops at $\gamma \lesssim 0.6$, it sticks to the hydrogel surface at a very early stage of its lifetime and its lower hemisphere significantly flattens as it grows and collapses, leaving only a thin liquid film between the two interfaces. In this case, the bubble assumes the shape of a cone and the ensuing microjet impinges almost directly onto the hydrogel. Between $\gamma \approx 0.8$ and 0.6 , we observe a gradual transition from the pear-shaped bubble to the cone-shaped bubble, highlighted in particular by the flattening of the lower hemisphere of the bubble. This transition between the two regimes is seemingly independent of the agarose concentration of the nearby boundaries.

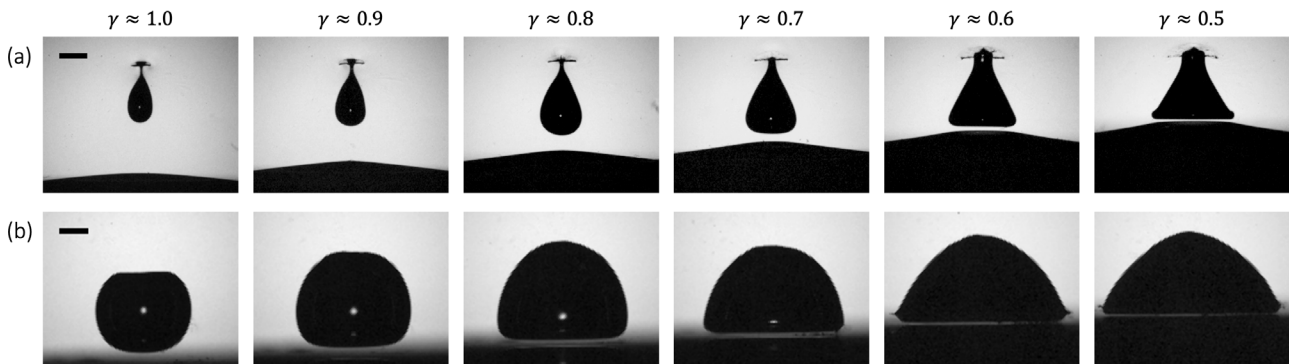


FIG. 3. (a) Snapshots of the bubble near the 2% (w/w) agarose hydrogel taken $0.2 \mu\text{s}$ before microjet formation and (b) snapshots of a similar bubble near a rigid boundary taken at the same time instant after bubble generation. The black line indicates the 1 mm scale.

A. Bubble dynamics

1. First oscillatory regime: $\gamma \gtrsim 0.8$

We show in Fig. 4 an overview of the dynamics of a cavitation bubble generated at $\gamma \approx 0.85$ near the 1% (w/w) and 3% (w/w) agarose hydrogels. The results of the numerical simulations are displayed in addition to the experimental observations for the first oscillation period of the bubble (left halves of the frames of Fig. 4). For both agarose concentrations, we observe excellent agreement between the spatiotemporal evolution of the experimental and numerical bubble profiles. The lower opacity of the hydrogel at a concentration of 1% (w/w) allows the visualization of the downward displacement of the hydrogel, which is consistent with the numerical simulations. The simulated upward displacements of the boundaries are also in good agreement with the experiments, although they are slightly overestimated. We believe that this is due to the fact that the Young’s modulus of agarose hydrogels is higher under tensile loading than under compressive loading,^{32,33,40} which we neglect in the numerical model. Given this close agreement, it is reasonable to use the BIM results as a complement to the experimental observations in order to shed further light on the dynamics of the bubbles.

Immediately after plasma generation, the bubble grows, retaining much of its spherical symmetry despite the presence of a nearby boundary [Fig. 4(a), frames 1–5]. The reason can be attributed to the downward compression of the elastic boundary which provides more room for the lower hemisphere of the bubble to expand downward, as opposed to a rigid boundary that would force the lower hemisphere to flatten and stretch along the boundary as evidenced on Fig. 3. We note here that a stiffer elastic boundary, i.e., a hydrogel with a higher agarose concentration, deforms less, therefore inducing a more notable flattening of the lower hemisphere of the bubble [Fig. 4(b), frames 1–5]. It is clear from the simulations that, by the time the bubble has reached its maximum volume, the boundary has already bounced back and is moving upward toward the bubble.

As the bubble begins its collapse phase, the boundary forms a distinctive mound and the bubble assumes a mushroom shape, characterized by a hemispherical cap and an indentation on the lateral sides [Figs. 4(a) and 4(b), frames 6–9]. The lateral walls of the bubble collapse faster than its upper or lower hemispheres and, eventually, it splits at the neck, triggering the simultaneous formation of an upward and downward microjet. The two remnant separated parts of the bubble then collapse, producing two distinct rebound bubbles. While the



FIG. 4. Bubble dynamics near different agarose hydrogels. (a) 1% (w/w) at $\gamma \approx 0.84$ and (b) 3% (w/w) at $\gamma \approx 0.83$. The interframe time is $75 \mu\text{s}$, and the black line indicates the 2 mm scale. The white dots indicate the position of the elastic boundary when compressed downward. The left halves of the frames 1–9 show the BIM results. The timing of the last simulation frame is slightly shifted to compare the bubble profiles close to the bubble collapse instant. This temporal adjustment corresponds to a maximum relative error of 1.2% with respect to the experiment.

lower rebound moves downward and collapses onto the elastic boundary, the upper part migrates away from the boundary [Figs. 4(a) and 4(b), frames 10–12]. Similar dynamics have been observed near other elastic boundaries and membranes.^{14,15,20}

Further insight into the pressure and velocity fields leading to these peculiar collapse dynamics is provided by the BIM simulations shown in Fig. 5, where the first row of each simulation is taken at the time when the bubble reached its maximum volume. At that instant,

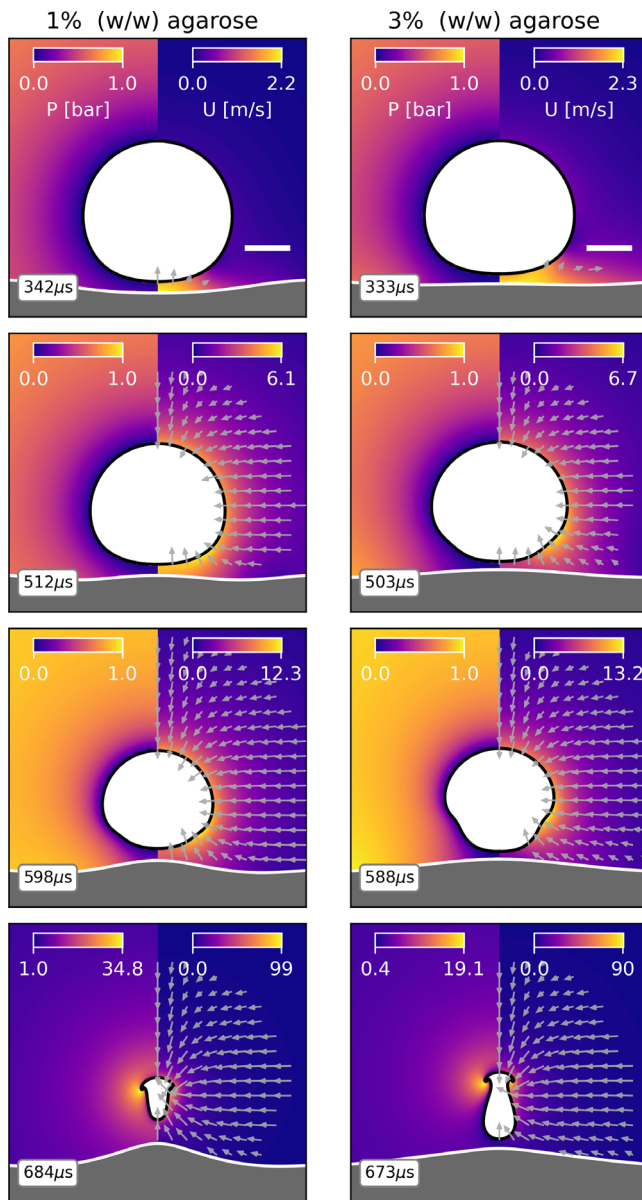


FIG. 5. BIM simulation of bubble collapse near hydrogels with 1% (w/w) and 3% (w/w) concentration at $\gamma = 0.85$. The first row of each simulation is taken at the time when the bubble reaches its maximum volume. The left halves of the images show the pressure field, and the right halves show the velocity field. The white line indicates the 2 mm scale.

the elastic boundary has already bounced back, thus inducing an upward flow field that pushes the bubble away from the boundary (Fig. 5, row 1). As the bubble continues to collapse, the elastic boundary moves upward likely due to a combined effect of the rebound of the surface and the formation of a low pressure region between the bubble and the hydrogel. The height and width of this hill depend essentially on the elasticity of the hydrogels, thus the hydrogel with the lower concentration forms a locally strongly deformed hill with high curvature, while the hydrogel with the higher concentration deforms more homogeneously. Furthermore, an annular liquid flow, parallel to the boundary, develops as the bubble shrinks (Fig. 5, rows 2–4). The combined effect of the upward flow triggered by the elastic boundary rebound, and the annular flow induced by the bubble collapse leads to the buildup of high velocity regions at the bottom of the bubble surface. This disturbance then moves along the sidewalls of the bubble toward its top, forming an indentation on the bubble lateral sides (Fig. 5, rows 2–3). Since the hydrogel with low elasticity deforms strongly but only locally, liquid flow under the bubble is possible. The bubble can therefore shrink considerably before its cap breaks. This is in contrast to the less compliant boundary, which impedes fluid flow beneath the bubble, ultimately delaying the collapse of its lower hemisphere. In this case, the bubble retains a larger volume when its cap breaks (Fig. 5, row 4). As the bubble dynamics following the cap rupture are not captured by the numerical simulations, we show high-speed imaging of the final instants of similar bubbles collapsing near the different investigated boundaries at $\gamma \approx 0.85$ in Fig. 6. First, as discussed above, it is evident from frame 1 that the agarose concentration of the hydrogels has a significant effect on the bubble volume during the final instants of its collapse, where bubbles developing over a stiffer hydrogel maintain a larger volume at the instant of cap rupture. This property of bubble–hydrogel interaction is maintained throughout the range of parameters investigated in this study. Near the 1% (w/w) and 2% (w/w) agarose hydrogels, the upward liquid flow triggered by the boundary elastic response induces the splitting of the bubble cap in two, thus forming a vapor ring [Figs. 6(a) and 6(b), frame 1]. The upper cap then collapses, shortly followed by the splitting of the bubble and the collapses of the annular ring [Figs. 6(a) and 6(b), frame 2]. For a bubble near the 1% (w/w) agarose hydrogel, the cap collapses approximately 400 ns before the bubble splits. Near the 2% (w/w) agarose hydrogel, the splitting precedes the cap collapse by about 200 ns. The same events, with different timings, take place for bubbles developing near the stiffer hydrogels. In that case, the splitting of the bubble occurs before the collapse of the cap, as shown by the timing of the shock waves [Figs. 6(c) and 6(d), frame 2]. For a bubble near the 3% (w/w) agarose hydrogel, both events occur less than a 100 ns apart, while for a bubble near the 4% (w/w) agarose hydrogel, the cap collapses about 300 ns after the bubble splitting. We note here that the splitting of the bubble appears to be the trigger for the formation of a downward microjet. The microjet then moves through the bubble and eventually pierces its lower hemisphere [Fig. 6(a), frames 2–4, and Fig. 6(b), frame 2–6]. The time lag between the microjet initiation and the bubble collapse is affected by the elasticity of the interfaces, with bubbles collapsing faster near the more compliant hydrogels. This aspect of the bubble behavior is quantified in Fig. 7 for the entire parameter space investigated in this study. The figure illustrates the time interval, Δt , from the microjet initiation to the bubble collapse, i.e., the minimum volume of the bubble. This time is normalized by twice the

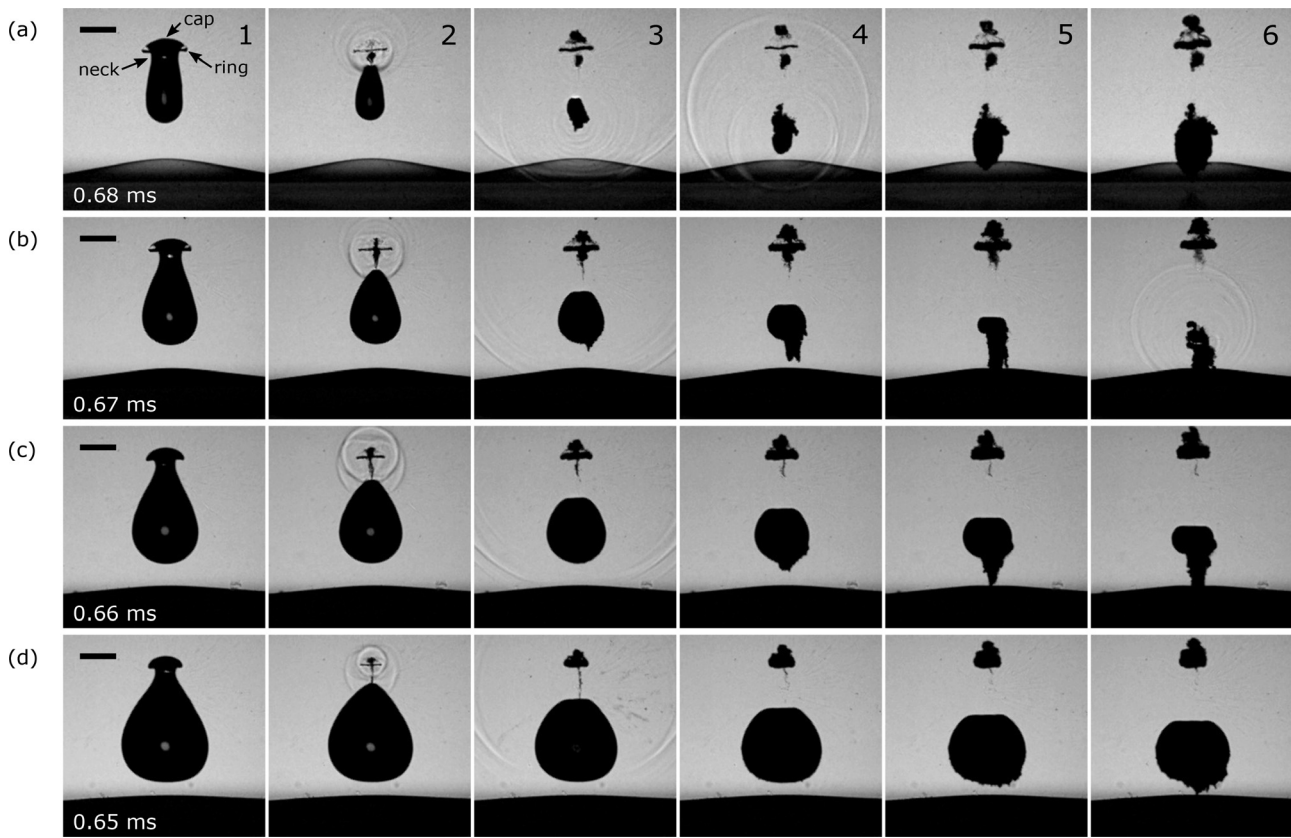


FIG. 6. Final instants of the bubble collapse near the different elastic boundaries. (a) 1% (w/w) at $\gamma \approx 0.84$, (b) 2% (w/w) at $\gamma \approx 0.86$, (c) 3% (w/w) at $\gamma \approx 0.85$, and (d) 4% (w/w) at $\gamma \approx 0.86$. The interframe time is $2 \mu\text{s}$, and the black line indicates the 1 mm scale.

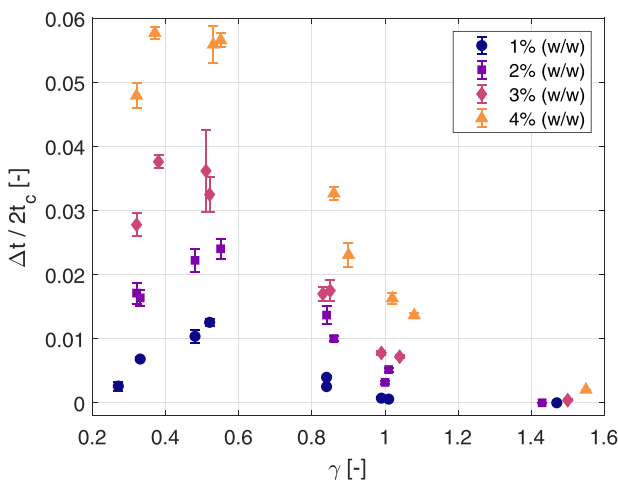


FIG. 7. Time interval from jet initiation to bubble collapse as a function of the standoff distance γ . The time is normalized by twice the Rayleigh collapse time of the corresponding unbounded bubble, $t_c = 0.915R_{\text{max}}[\rho/(p_0 - p_v)]^{0.5}$. The markers correspond to the various agarose hydrogels: indigo filled circle 1% (w/w), purple filled square 2% (w/w), pink filled diamond 3% (w/w), and orange filled triangle 4% (w/w). The error bars show the standard deviation of the measurements.

Rayleigh collapse time, $t_c = 0.915R_{\text{max}}[\rho/(p_0 - p_v)]^{0.5}$, of the corresponding unbounded bubble. It can be seen that not only does the time interval from jet initiation to bubble collapse increase with the elasticity of the boundary, but it also increases with a decrease in the standoff distance until a maximum is reached at $\gamma \approx 0.5$.

2. Second oscillatory regime: $\gamma \leq 0.6$

When the bubble is generated closer to the boundary, the interactions between the cavity and the elastic interface are stronger, leading to bubble dynamics that are noticeably different from those described above. We illustrate these dynamics in Figs. 8–10, which show a bubble interacting with the various interfaces considered at $\gamma \approx 0.55$. Figure 8 gives an overview of the lifetime of the bubble near the hydrogels at 2% (w/w) and 4% (w/w) agarose concentration. As before, we overlay this figure with the results of the BIM simulations. We observe close agreement between the experimental observations and the predictions of the numerical model. It should however be mentioned that the model underestimates the film thickness between the bubble and the hydrogel. This discrepancy may be due to the fact that the BIM neglects the fluid viscosity, the effects of which can become important when the bubble develops this close to a boundary. The upward displacement of the boundary is also overestimated, which, as mentioned

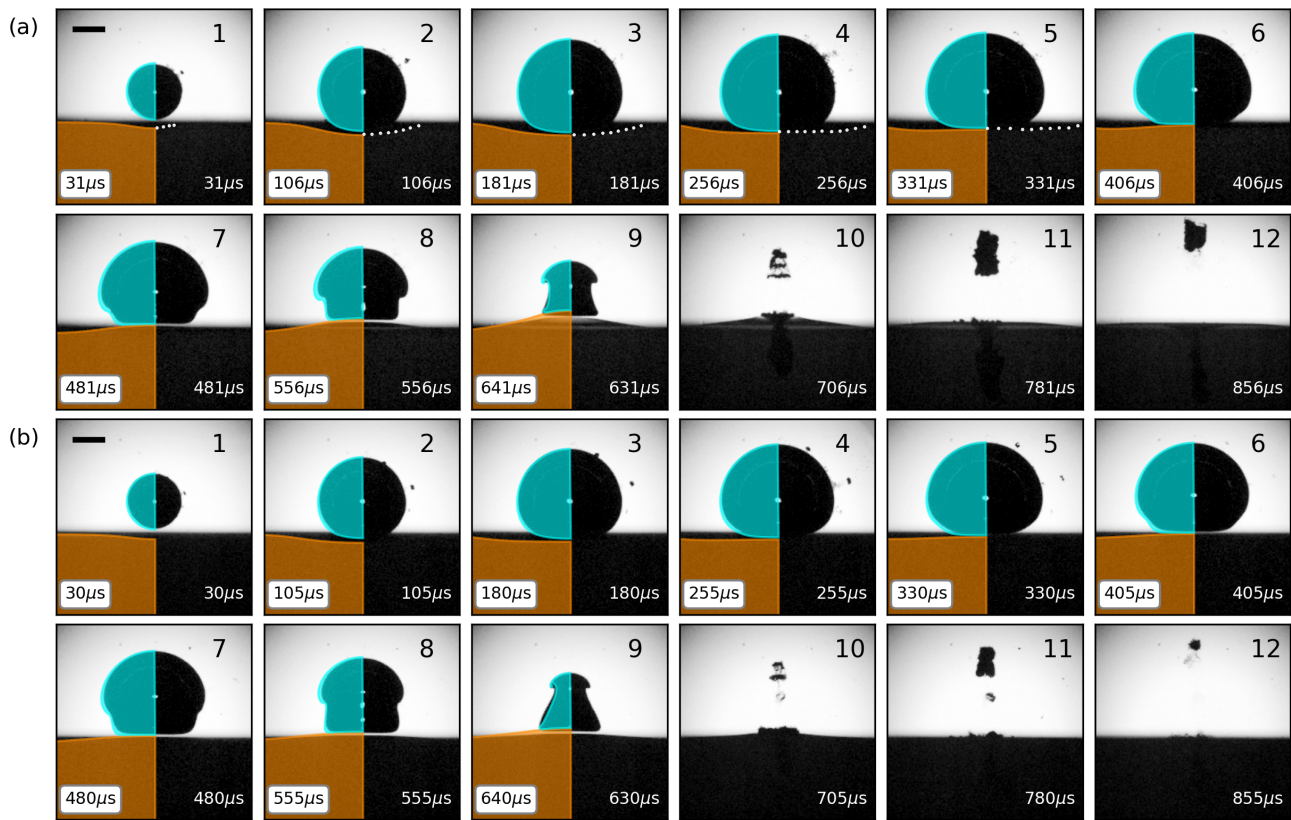


FIG. 8. Bubble dynamics near the different agarose gels. (a) 2% (w/w) at $\gamma \approx 0.52$ and (b) 4% (w/w) at $\gamma \approx 0.55$. The interframe time is $75 \mu\text{s}$, and the black line indicates the 2 mm scale. The white dots indicate the position of the boundary when compressed downward. The left halves of the frames 1–9 show the BIM results. The timing of the last simulation frame is slightly shifted to compare the bubble profiles close to the bubble collapse instant. This temporal adjustment corresponds to a maximum relative error of 1.6% with respect to the experiment.

above, could be due to the Young’s modulus of the hydrogel being higher under tensile loading than under compressive loading, a factor that has not been taken into account in the BIM. The simulations however provide valuable information about the hydrogel’s downward deformation and the bubble’s lower hemisphere dynamics, which are concealed in the experimental visualizations during the bubble growth. We note that extended image processing (not shown in this work) enabled us to detect the interface of the compressed 2% (w/w) agarose hydrogel. Whenever possible, we therefore show the position of the elastic boundary with white dots in Fig. 8 and observe a close agreement.

Immediately after its formation, the bubble pushes against the elastic boundaries, which deform under the applied pressure field (Fig. 8, frames 1–4). Unsurprisingly, the stiffer hydrogel deforms less and springs back sooner, significantly preventing the lower hemisphere of the bubble from expanding downward, as opposed to a softer hydrogel, which deforms more. After the bubble has reached its maximum volume, it collapses (Fig. 8, frames 6–9). Only a thin film of liquid is visible between the hydrogel and the bubble, which impedes the fluid flow from underneath of the bubble and essentially prevents the collapse of its lower hemisphere. In addition, the side walls of the bubble collapse faster than its upper hemisphere, so that the bubble takes on a

mushroom shape as the collapse progresses. Eventually, the cap of this mushroom-shaped bubble collapses. This results in the formation of a microjet that travels through the bubble and penetrates the hydrogel (Fig. 8, frames 9–10). The process is accompanied by the ejection a small vapor cavity that moves away from the boundary (Fig. 8, frames 10–12).

Further insight into the pressure and velocity fields associated with the bubble collapse is provided in the numerical simulations, as shown in Fig. 9. The figure illustrates the collapse phase of the bubbles near the agarose hydrogels with 2% (w/w) and 4% (w/w) agarose concentration. The first row of Fig. 9 is taken at the time when the bubbles reach their maximum volume. At this stage, the previously compressed elastic boundaries have already bounced back, pushing the bubbles upward and transferring their momentum to the surrounding fluid. Concurrently, a high-velocity region forms near the bubble bottoms. At this stage, the onset of an indentation is visible at the bottom of the bubble sidewalls. As the bubble continues to collapse, the boundary’s rebound and the contraction of the bubble’s sidewalls result in an upward and annular flow, respectively. The combined effect of these two flows causes the indentation on the sidewalls of the bubble to become more prominent and move upward along the bubble interface (Fig. 9, frame 2–3). The bubble eventually assumes this typical

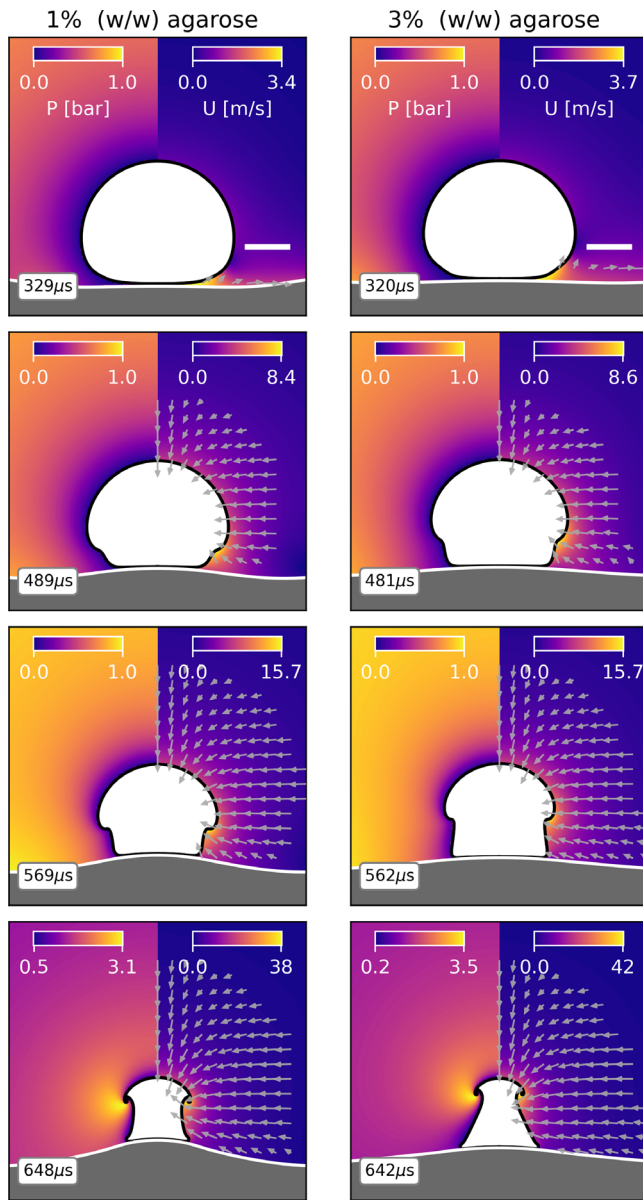


FIG. 9. BIM simulations of bubbles collapse near hydrogels with 1% (w/w) and 3% (w/w) agarose concentration at $\gamma = 0.55$. The first row of each simulation is taken at the time when the bubble reaches its maximum volume. The left half of the images shows the pressure field, and the right half shows the velocity field. The white line indicates the 2 mm scale.

mushroom shape, which has already been described in various studies investigating the interaction of cavitation bubbles with elastic interfaces.^{14,15,20,25} Ultimately, the upward flow of the liquid causes the cap to split and release a vapor vortex ring (Fig. 9, frame 4). As before, a detailed description of the events following the splitting of the cap is not captured by the numerical simulation. Instead, we show in Fig. 10 high-speed imaging of the final instants of the bubble collapsing near the four investigated agarose hydrogels at $\gamma \approx 0.55$. The first frame in

Fig. 10 is taken shortly after the separation of the vortex ring from the cap of the mushroom-shaped bubble. The remainder of the hemispherical cap then collapses inward (Fig. 10, frame 2), initiating a microjet that propagates through a now conical bubble and pierces the nearby boundary (Fig. 10, frames 3–4). We note that the size of the conical bubble depends strongly on the elasticity of the agarose hydrogel, with a stiffer boundary leading to a larger bubble at the time of the microjet onset. This is probably due to a higher but narrower volcano-shaped deformation of the softer elastic boundaries, which therefore impede the fluid flow below the bubble over a smaller area. The rest of the bubble then collapses. The time interval between the onset of the microjet and the collapse of the bubble is inversely proportional to the size of the conical bubble as shown in Fig. 10, frames 4–6, and quantified in Fig. 7.

B. Microjets dynamics

We now focus our attention on the dynamics of the microjets. The location and instant at which the microjets are triggered varies according to the two previously identified oscillatory regimes. In the regime defined by $\gamma \leq 0.6$, we find that the collapse of the spherical cap shortly precedes the formation of the microjet, while at $\gamma \geq 0.8$ the closure of the neck appears to be the precursor. We believe both initiating events can be attributed to an annular inflow of liquid at the axis of symmetry, which generates a shock wave in the liquid phase when it collides with itself. We highlight these two mechanisms on Fig. 11, which shows a cavitation bubbles collapsing near the 2% (w/w) agarose hydrogel at two different standoff distances, using a frame-difference technique. The color map of the image is normalized between 0 and 1, with higher values corresponding to a larger grayscale difference between two consecutive images. Figures 11(a) and 11(b) therefore highlight the evolution in time of the boundary position of the bubble immediately before the neck closure at $\gamma \approx 0.86$ and the cap collapse at $\gamma \approx 0.55$, respectively. The following bubble dynamics are depicted in Fig. 12 (Multimedia view), which shows the final phase of bubbles collapsing near the 3% (w/w) agarose hydrogel, recorded using a diffuse light technique, where each row refers to a specific γ . The first frame shows the moment of closure of the neck [$\gamma \approx 1.0$ in Fig. 12(a), and $\gamma \approx 0.86$ in Fig. 12(b)], or collapse of the cap [$\gamma \approx 0.55$ in Fig. 12(c), and $\gamma \approx 0.32$ in Fig. 12(d)]. This instant is set at time $t = 0$ on the figure. Immediately after the annular inflow of the liquid collides on itself, a zone of strong curvature is left on the upper hemisphere of the bubble (Fig. 12, frame 1). The strongly curved region finally retracts inward and the microjet forms. This jet appears to initially consists of a spray of atomized microdroplets that spread along the symmetry axis of the bubble as well as radially outward (Fig. 12, frames 2–5). At $\gamma \approx 1.0$ and $\gamma \approx 0.86$, the microdroplets impinge on the bubble walls, resulting in capillary waves that ripple across its interface [Figs. 12(a) and 12(b), frame 5]. This phenomenon leads to chaotic refraction of light at the bubble wall and prevents a clear view of its interior. For this reason, the events that follow the spraying of microdroplets are more challenging to identify. However, an intact round liquid microjet can be roughly detected despite the ripples at the bubble boundary. At $\gamma \approx 0.86$, for example, this liquid microjet is visible in the upper part of the bubble [Fig. 12(b), frames 4–6]. Hence, the initially atomized jet appears to stabilize into a round liquid microjet as the bubble further collapses. Eventually, the liquid microjet pierces the bottom of the bubble and continues its path in the water.

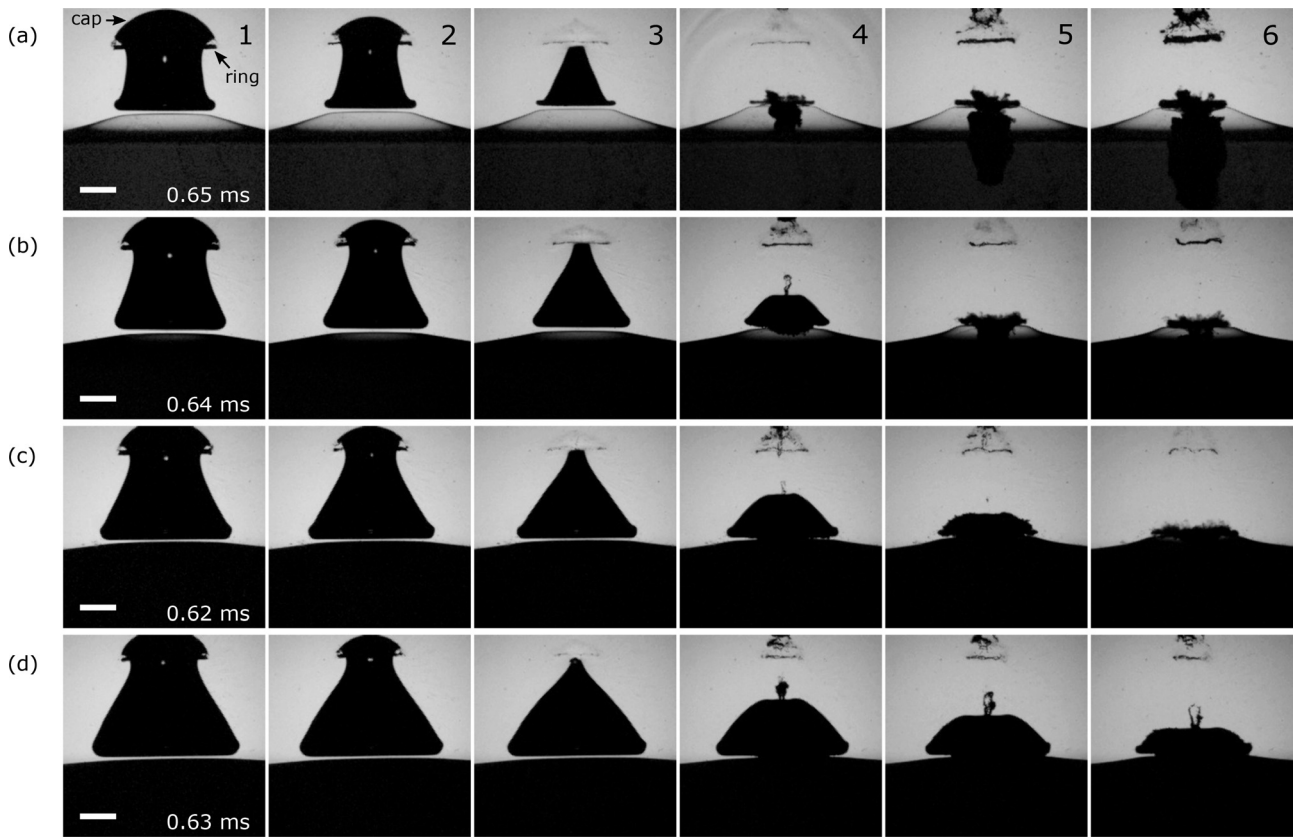


FIG. 10. Final instants of the bubble collapse near the different elastic boundaries. (a) 1% (w/w) at $\gamma \approx 0.52$, (b) 2% (w/w) at $\gamma \approx 0.55$, (c) 3% (w/w) at $\gamma \approx 0.52$, and (d) 4% (w/w) at $\gamma \approx 0.53$. The interframe time is $8 \mu\text{s}$, and the white line indicates the 1 mm scale.

At $\gamma \approx 0.55$ and 0.32 , the visibility of the bubble interior is not affected by the spray [Figs. 12(c) and 12(d), respectively]. This is due to a seemingly narrower propagation angle of the atomized portion of the jet, such that the droplets mainly impinge on the lower bubble

wall. The interior of the bubble is therefore more visible until the end of the collapse, and the water microjet is clearly identifiable [Figs. 12(c) and 12(d), frames 4 and 5, respectively]. After piercing the bubble's lower hemisphere, the liquid microjet almost immediately

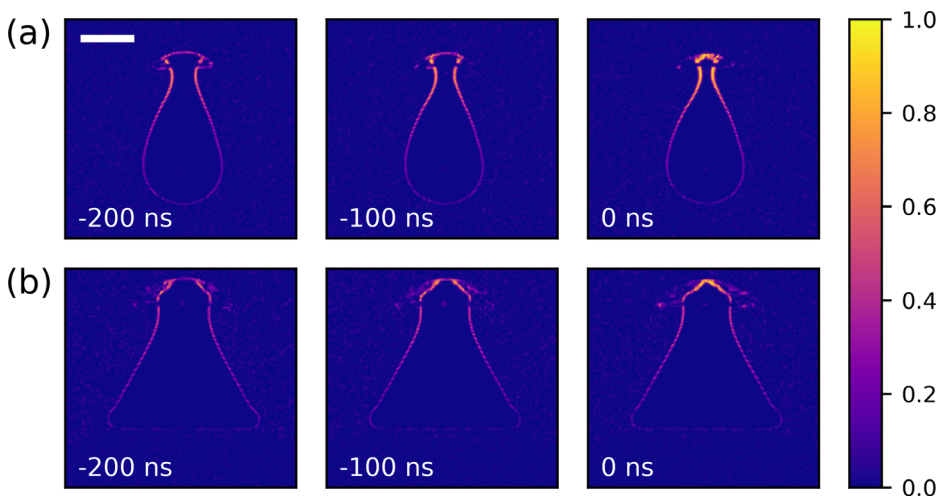


FIG. 11. Time-difference images of single cavitation bubbles collapsing near 2% (w/w) agarose hydrogel at (a) $\gamma = 0.86$ and (b) $\gamma = 0.55$. The time $t = 0 \text{ ns}$ is set a few instants before the cap collapse. Images are extracted from shadowgraphs recorded at $10 \times 10^6 \text{ frames s}^{-1}$. The color code refers to the normalized grayscale difference between two sequential images. The grayscale difference is normalized by the maximum value of each sequence. The white line indicates the 1 mm scale.

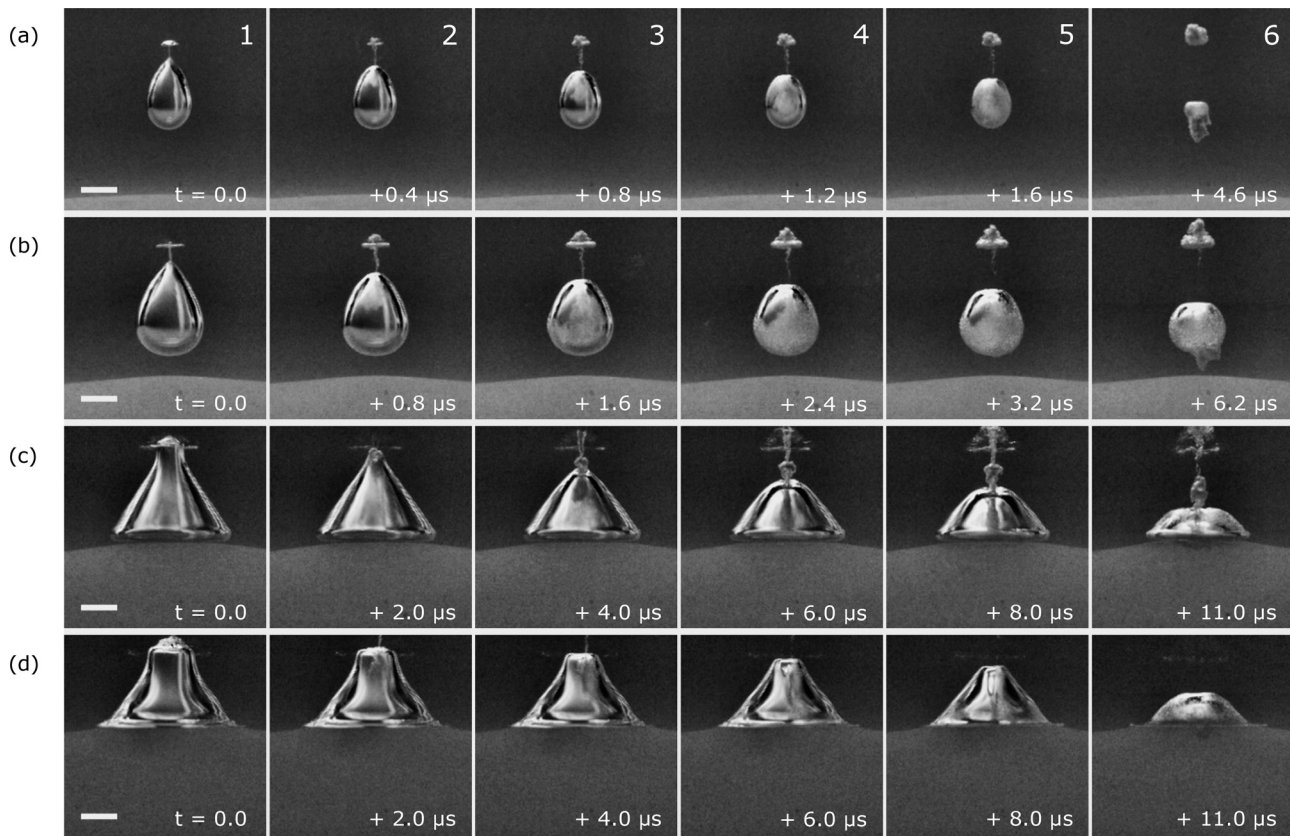


FIG. 12. Final instants of the bubble collapse near a 3% (w/w) agarose hydrogel recorded with a diffused-light technique. (a) $\gamma \approx 1.00$, (b) $\gamma \approx 0.86$, (c) $\gamma \approx 0.55$, and (d) $\gamma \approx 0.32$. The interframe time varies among the different cases to account for longer collapse time at smaller standoff distances. All snapshots are extracted from 10×10^6 frames s^{-1} recordings. The white lines indicate the 1 mm scale. Multimedia views: <https://doi.org/10.1063/5.0136577.1>; <https://doi.org/10.1063/5.0136577.2>; <https://doi.org/10.1063/5.0136577.3>; <https://doi.org/10.1063/5.0136577.4>

punctures the agarose hydrogel surface, which lies directly under a thin layer of water that separates it from the bottom of the bubble [Figs. 12(a) and 12(b), frames 5–6]. Regardless of the regime considered, we note that the round liquid jet appears to be the main cause of piercing of the bubble surface and agarose hydrogels, rather than microdroplets originating from the atomized tip of jet.

We show in Fig. 13(a) the velocity of the liquid microjet and in Fig. 13(b) the velocity of the atomized portion of the jet as a function of distance γ for the bubbles developing near the different investigated boundaries. These velocities are measured using the 10×10^6 frame s^{-1} visualizations. The velocity of the atomized portion of the jet is determined by tracking its position within the bubble and measured between two points as far apart as possible. Since the bubble walls are locally curved, our velocity estimate takes into account the optical refraction at the bubble surface using Snell's law. Alternatively, the velocity of the liquid water microjet is determined from both the shadowgraphs and the diffuse light visualizations. We estimate this velocity by measuring the distance the microjet travels between its onset and the piercing of the opposite bubble wall. In the shadowgraphs, the formation of the microjet is preceded by a shock wave, so that the onset of the microjet is well defined. In diffuse light visualization, we assume that the inception of the microjet occurs one frame ($0.1 \mu s$ in 10×10^6 frame s^{-1})

before the atomized microjet is detected within the bubble. In both cases, the penetration of the opposite bubble wall is well defined. The details regarding the uncertainties associated with these measurements are provided in Appendix B. As shown in Fig. 13, the velocity of both type of microjets is strongly affected by the standoff distance γ . At larger γ , the jets tend to higher speeds. Based on the available data, the spray jet velocity of bubbles developing near 2% (w/w) and 3% (w/w) agarose hydrogels appears to reach a maximum between $\gamma \approx 1$ and 0.8. An identical trend is observed for the fully liquid microjet of a bubble near the 2% (w/w) gels. As in the other test cases studied, the velocities of the microjets decrease as the standoff distance is reduced. The jets velocities is also significantly affected by the agarose concentration of the nearby boundaries, with more flexible hydrogels generally leading to higher microjet speeds. We note here that, around $\gamma \approx 0.5$, the liquid microjet velocity tends to similar value, regardless of the elasticity of the boundary. We also note that the atomized jets reach significantly higher velocities than the associated liquid jets, being about twice as fast. The maximum measured velocity of the atomized portion of the jet is about 2000 ms^{-1} for a bubble collapsing at $\gamma \approx 0.8$ near the 1% (w/w) agarose hydrogel. Under the same conditions, the liquid microjet propagates with a velocity of 1000 ms^{-1} inside the bubble. Assuming that the bubble is

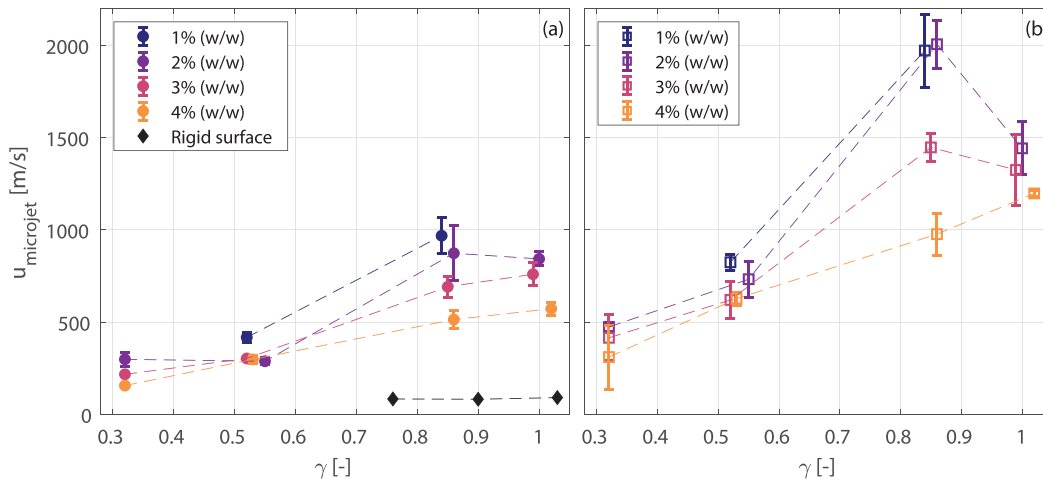


FIG. 13. Average microjet speed of the liquid microjet (a) and the atomized microjet (b). The filled circles refer to the average speed of the liquid microjet: indigo filled circle 1% (w/w), purple filled circle 2% (w/w), pink filled circle 3% (w/w), and orange filled circle 4% (w/w), whereas the hollow squares refer to the average speed of the atomized jet: indigo square 1% (w/w), purple square 2% (w/w), pink square 3% (w/w), and orange square 4% (w/w). The error bars show the standard deviation of the measurements. The black diamonds refer to the average speed of the liquid jet developing in a bubble close to a rigid surface. The data are linearly interpolated (dashed lines) to facilitate the plot readability.

filled with water vapor at ~ 2300 Pa which behaves according to an ideal gas law, both atomized and liquid microjets can reach supersonic velocities. The fastest liquid microjet travels at a Mach number $Ma \approx 2.4$ and the fastest spray at $Ma \approx 4.7$.

IV. DISCUSSION

Anisotropies in the liquid pressure field generally lead to an aspherical collapse of the bubble. When the anisotropy is characterized by a unidirectional pressure gradient, such as in the case of a bubble oscillating near a solid boundary or a free surface, the bubble's hemisphere exposed to the highest pressure collapses faster, resulting in an involution of that hemisphere and the formation of a microjet that travels along the bubble's axis of symmetry. This mechanism is different from the one described in Sec. III B, where the microjets are initiated following a fast contraction of the bubble sidewalls, evidenced either by the closure of the bubble's neck or the collapse of its spherical cap. This difference is highlighted in Fig. 3 for bubbles generated at $\gamma \approx 1.0$, where the neck of the bubble near the elastic boundary is about to collide and trigger the microjet, while the upper hemisphere of the bubble near a rigid surface is already flattened, indicating that the microjet has formed. The velocity of the microjet measured for bubble close to hydrogels is also significantly higher than the one measured close to a rigid boundary, as shown in Fig. 13. The mechanisms leading to such a fast microjet have already been discussed in the literature, and we summarize the main findings hereafter. Brujan *et al.*¹⁴ reported similar dynamics of cavitation bubbles near PAA hydrogels and noted the occurrence of high-speed needlelike jets ($\sim 960 \text{ ms}^{-1}$) following the splitting of the bubbles. They attributed the high velocity of the microjets to a focusing of the liquid flow from a large solid angle into a thin liquid jet. We find that the microjet diameter of the bubble collapsing at $\gamma \approx 0.86$ near the 2% (w/w) agarose hydrogel is approximately $150 \mu\text{m}$, while that of a similar bubble collapsing near a rigid boundary has a diameter of about $700 \mu\text{m}$. This leads to an

approximately 20-fold difference in the cross-sectional area of the microjets, which could explain the velocity difference through the argument of flow focusing. In addition, the authors argued that the impact of shock waves onto the lower half of the split cavity also contributes to the high velocity of the microjets. An example of this impact is clearly evidenced on frame 2 in Figs. 6(a)–6(d). We further highlight this mechanism in Fig. 14(a), which illustrates the bubble behavior instantly after the collapse of its neck at $\gamma \approx 0.86$ near the 2% (w/w) hydrogel. The right halves of the frames are shadowgraphs, and the left halves are diffuse light visualizations taken at the same instants. This direct comparison is made possible because of the high repeatability of the bubble we generate. It is clear from these visualizations that a shock wave impacts the bubble upper hemisphere within the 200 ns that follow the bubble necking. On the following frames, the atomized portion of the jet is seen traveling through the bubble. The jet travels faster than the shock wave, as seen in this visualization and reported in Fig. 13. Figure 14(b) shows the velocity of the shock wave as a function of the distance traveled since its inception. We measured this velocity by fitting circles to the shock wave front and evaluating the change in radius between two successive images with a time interval of 100 ns. Our measurements indicate that the shock wave travels at a supersonic speed of about 2170 ms^{-1} in the initial phase of its propagation and eventually reaches the speed of sound in water at atmospheric pressure and 25°C of about 1500 ms^{-1} as it propagates further. Considering that the impingement of a shock wave on the cavity contributes to the high velocity of the microjet, the occurrence of a supersonic wave could indeed be one of the reasons why the atomized jet is accelerated to such high velocities. Through a comparison with shaped charge dynamics, Brujan *et al.*¹⁴ moreover pointed out that the conical shape assumed by the cavity allowed the jet to accelerate as it moves through the bubble. Alternatively, we note that the mechanism that triggers the microjet of a bubble collapsing near an elastic boundary bears similarities to the one identified by Lechner *et al.*⁴¹ for

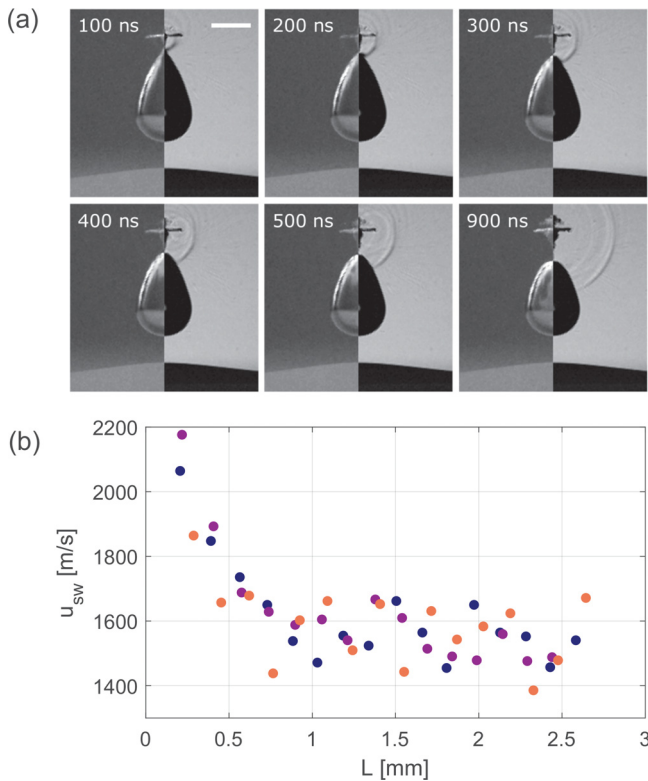


FIG. 14. (a) Snapshots of the instants following the neck closure of a bubble at $\gamma \approx 0.86$ near the 2% (w/w) agarose hydrogel. Left halves of the frames are diffused light visualizations, and the right halves of the frames are shadowgraphs taken at the same instant (the time $t=0$ is taken at the instant of neck closure). The white line indicates the 1 mm scale. (b) Velocity of the shock wave emitted upon neck closure as a function of distance from its point of origin. The various markers (indigo filled circle, purple filled circle, and orange filled circle) indicate measurements made on three distinct bubbles in the same condition.

bubbles collapsing in extreme proximity to a solid surface ($\gamma \leq 0.2$). Their numerical simulations indeed revealed an annular inflow of liquid that develops at the upper hemisphere of the bubble when it collapses. The subsequent liquid collision generates a shock wave in the liquid phase resulting in a very high and localized pressure zone that drives a thin microjet through the bubble ($\sim 1000 \text{ ms}^{-1}$). A pressure surge following the collision of the converging fluid flow was also numerically identified by Pishchalnikov *et al.*⁴² in the case of an acoustically driven micro-bubble collapsing in contact with a rigid surface. We therefore believe that the main mechanism contributing to the formation of the high-speed microjets described in Sec. III B can reasonably be attributed to a combination of the aforementioned effects, namely, (i) a strong flow focusing acting on a very small and highly curved region on the upper hemisphere of the bubble, (ii) a pressure surge resulting from the annular inflow impinging on itself, and (iii) an interaction with shock waves emitted upon the neck closure or cap collapse.

The breakup of the high-speed microjet into droplets was also reported in the numerical work of Lechner *et al.*⁴¹ This observation was moreover confirmed experimentally by Reuter and Ohl,⁴³ who

observed a fragmented microjet hitting the bottom of a bubble developing extremely close to solid boundary. Although we provide strong time-resolved evidence for the microjet atomization in this work, we cannot unambiguously determine the mechanism responsible for the jet breakup based on our experimental observations alone. However, we propose the following hypotheses as possible explanations. The stability of a liquid jet flowing from a nozzle can be, in part, characterized by the vapor Weber number which represents the ratio between the fluid disruptive inertia forces and the stabilizing surface tension forces. It is expressed as $We_g = \rho_g du_{jet}^2 / \sigma_v$, where ρ_g is the density of the gas within which the jet with diameter d and velocity u_{jet} flows, and σ_v is the surface tension of water in contact with its vapor. Even though a liquid jet is inherently unstable and can breakup into drops,⁴⁴ a large Weber numbers generally indicate a high instability of the liquid interface of the jet.⁴⁵ A qualitative classification of jet instability regimes was discussed in the review of Lin and Reitz.⁴⁴ Based on this classification, the jet atomization regime is argued to occur for $We_g > 40.3$. This regime is characterized by the disintegration of the jet into droplets as soon as it exits the nozzle. At smaller Weber number, $13 > We_g > 40.3$, the regime is referred to as second-wind-induced. This regime is also characterized by the breakup of the jet into droplets, except that the breakup is initiated downstream of the nozzle exit. Although these regimes have been identified for steady-state jets exiting nozzles, it is not unreasonable to analyze the microjets observed in this work in terms of Weber number to explain their atomization. We assume that the bubble is exclusively filled with water vapor at $\sim 2300 \text{ Pa}$ which behaves according to an ideal gas law. The gas density within the bubble is thus obtained with $\rho_g = p_v / (RT) \approx 17 \text{ g/m}^3$, where $R = 461.5 \text{ J kg}^{-1} \text{ K}^{-1}$ is the specific gas constant for water vapor and T is taken as approximately 298.15 K . We take $\sigma_v = 73 \times 10^{-3} \text{ N/m}$ for the surface tension of water in contact with its vapor.⁴⁶ The diameter of the jets is about $150 \mu\text{m}$ at $\gamma \approx 0.86$. Thus, the Weber number for the fastest measured liquid microjet is $We_g \approx 35$, and, if we consider instead the velocity of the atomized part of the same jet, we obtain $We_g \approx 140$. Consequently, both these microjets belong to a regime where a breakup into droplets may be expected. For comparison, the microjet of a similar bubble collapsing near a rigid boundary is characterized by a Weber number of $We_g \approx 1.1$. This significant difference could therefore explain why we observe an initial atomization of the microjet of a bubble collapsing near an elastic surface, but not in the case of a similar bubble near a rigid boundary.

Another explanation for the microjet atomization could result from its interactions with the shock waves generated when the bubble neck closes or its cap collapses. This hypothesis is derived from the following consideration. When an interface between two fluids is struck by a shock wave, it is impulsively accelerated in the same direction as the incoming shock wave. We can cite here the example of a gaseous bubble, initially at rest a liquid, impacted by a shock wave. The shock wave causes the struck side of the bubble to accelerate and to eventually form a jet of liquid directed at the other side of the bubble.⁴⁷ If we now consider that the gas-liquid interface exhibits an initial perturbation on its surface, the passage of the shock wave may lead to an increase in this perturbation over time, a phenomenon known as the Richtmyer–Meshkov instability.⁴⁸ The increase in perturbation could then produce more distortion at the interface and promote the formation of secondary instabilities, such as the Kelvin–Helmholtz shearing

instability,⁴⁹ which in turn could foster the breakup of the liquid microjet into droplets. Therefore, it is not unreasonable to hypothesize that the shock waves interacting with the microjet not only contributes to its development, but also plays a role in its atomization. An example of these interactions is shown on frame 2 in Figs. 6(a)–6(d).

The two hypotheses discussed above have merit, and the mechanism responsible for microjet atomization could be a combination of both. It however must be noted that other mechanism could play a role in jet atomization. Among them, it is worth mentioning that a sudden vaporization of the tiny microjet within the rarefied bubble atmosphere would likely contribute to its destabilization and atomization. A definitive answer could be found through high-speed visualization with higher spatial and possibly temporal resolution, focusing on the location of microjet initiation. Alternatively, numerical simulation could also provide additional information beyond the reach of the current experimental observations.

V. CONCLUSION

In this study, we used high-speed imaging to investigate the dynamics of a laser-induced cavitation bubble near agarose hydrogels with different degrees of elasticity. Based on the standoff distance γ , we identified two main regimes for the bubble oscillations. In the first regime ($\gamma \geq 0.8$), the bubble takes the shape of a pear when it collapses, and a downward microjet forms at the closure of the bubble's neck. In the second regime ($\gamma \leq 0.6$), the bubble assumes the shape of a cone in the final moments of its collapse, and the downward microjet is initiated when the spherical cap on the upper hemisphere of the bubble collapses. Time-resolved visualizations of the interior of the bubble showed an initial atomization of these microjets that precedes to the formation of a fully liquid microjet traveling through the bubble. The velocity of both types of microjets depends strongly on the standoff distance and elasticity of the hydrogel. We suggest that the atomization of the microjet is likely due to (i) instabilities resulting from its high velocity and interaction with shock waves and (ii) possible evaporation of the thin microjet in the rarefied atmosphere within the bubble. To gain further insight into the bubble dynamics, we proposed a numerical model based on the boundary integral method. We modeled the agarose hydrogel as a liquid with a surface tension derived from the actual mechanical properties of the hydrogel. Despite the simplicity of the numerical model, the simulations are in a remarkable agreement with the experimental observations and fairly reproduce the growth and collapse of the bubble as well as the deformation of the hydrogel.

ACKNOWLEDGMENTS

A.B.S. acknowledges the financial support of the Swiss National Science Foundation under Grant No. 179018. D.B.P. acknowledges the funding for this work provided by the MSCA-ITN-ETN of the European Union's H2020 program under REA Grant Agreement No. 813766. The authors would like to thank I. Rivens and L. Braunstein (Institute of Cancer Research, London) for their suggestions regarding the hydrogels preparation, and the Soft Materials Laboratory (EPFL) for their assistance with the hydrogels mechanical tests. The authors would also like to thank O. Supponen (Institute of Fluid Dynamics, ETH Zürich) for the insightful discussions and valuable suggestions.

AUTHOR DECLARATIONS

Conflict of Interest

The authors have no conflicts to disclose.

Author Contributions

Armand Baptiste Sieber: Conceptualization (equal); Formal analysis (equal); Methodology (equal); Software (lead); Validation (equal); Visualization (equal); Writing – original draft (equal); Writing – review & editing (equal). **Davide Bernardo Preso:** Conceptualization (equal); Formal analysis (equal); Methodology (equal); Software (supporting); Validation (equal); Visualization (equal); Writing – original draft (equal); Writing – review & editing (equal). **Mohamed Farhat:** Conceptualization (equal); Formal analysis (equal); Funding acquisition (lead); Methodology (equal); Project administration (lead); Supervision (lead); Writing – review & editing (equal).

DATA AVAILABILITY

The data that support the findings of this study are available from the corresponding author upon reasonable request.

APPENDIX A: SURFACE TENSION AND YOUNG'S MODULUS RELATIONSHIP

We propose an energy-based approach to relate the hypothetical surface tension used in the numerical model to the actual elastic properties of the agarose hydrogel.

To this end, let us first consider a semi-infinite medium, representative of the agarose hydrogel and characterized by a Young's modulus E and a Poisson's ratio ν . We then suppose that the pressure load produced by the cavitation bubble upon the solid can be replaced by an axisymmetric pressure distribution of the form $p(r) = p_h(1 - r^2/a_c^2)^{0.5}$. The pressure distribution has a maximum value p_h and acts on a circular region of radius a_c perpendicular to the material surface. In a quasi-static framework and assuming small strains so that linear elasticity holds, the vertical displacement of the surface resulting from the applied load is given by⁵⁰

$$u_z(r) = \frac{\pi p_h}{4E^* a_c} (2a_c^2 - r^2), \quad r \leq a_c, \quad (A1)$$

where $E^* = E/(1 - \nu^2)$. The pressure $p(r)$ also corresponds to the Hertzian pressure,⁵¹ which is the normal pressure distribution resulting from the indentation of a solid sphere of radius R_i at a depth d_i in an elastic half-space. If the radius R_i is large compared to the contact radius a_c , the deformation within the contact region can be approximated by a parabola and the quadratic distribution of the vertical displacement, u_z , is expressed as^{50,52}

$$u_z(r) = d_i - \frac{r^2}{2R_i}, \quad r \leq a_c, \\ u_z(r) = \frac{a_c^2}{\pi R_i} \left[\left(2 - \frac{r^2}{a_c^2} \right) \arcsin \left(\frac{a_c}{r} \right) + \frac{\sqrt{r^2 - a_c^2}}{a_c} \right], \quad r > a_c. \quad (A2)$$

Combining Eqs. (A1) and (A2), we obtain $a_c^2 = R_i d_i$ and $p_h = (2/\pi)E^*(d_i/R_i)^{0.5}$. The associated normal force is given by

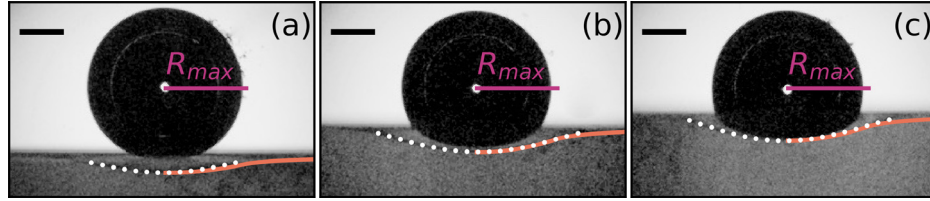


FIG. 15. Maximum deformation of the 1% (w/w) agarose hydrogel caused by a bubble generated at (a) $\gamma \approx 0.84$, (b) $\gamma \approx 0.48$, and (c) $\gamma \approx 0.35$. The solid line (orange solid line) represents the deformation fitted with Eq. (A2), and the white dots highlight the actual deformation of the agarose hydrogel. The black line indicates the 2 mm scale.

$F_N(d_i) = 4/3E^*R_i^{0.5}d_i^{1.5}$, and the potential energy stored in the elastic deformation can be derived as^{50,52}

$$U_E = \int_0^{d_i} F_N(\tilde{d})d\tilde{d} = \frac{8}{15}E^*\sqrt{R_id_i^5}. \quad (A3)$$

To evaluate the validity of the hypotheses made so far, we superimpose in Fig. 15 the surface deformation predicted by Eq. (A2) with the actual deformation of the 1% (w/w) agarose hydrogel caused by a bubble generated at $\gamma \approx 0.84, 0.48$, and 0.35 . All three images in Fig. 15 were taken at the time when the downward compression of the hydrogel reaches its maximum and briefly stops moving. The value of d_i is fitted to our experimental observations, a_c is taken as the maximum bubble radius $R_{max} = 3.7$ mm, which we consider a reasonable approximation in the case of a bubble oscillating near a boundary, and R_i is derived from the relation $a_c^2 = R_id_i$. Satisfactory agreement in surface deformation is observed for all three images, indicating that the stored potential energy given by Eq. (A3) is probably also a fair estimate.

Alternatively, let us now consider the agarose hydrogel to be a liquid with a surface tension σ , as in the numerical simulations. In that case, the displacement described in Eq. (A2) leads to an

increase in the surface area, ΔA , which is associated with an increase in the surface potential energy, $U_\sigma = \sigma\Delta A$. The change in surface area is obtained as

$$\Delta A = \lim_{b \rightarrow \infty} \left(2\pi \int_0^b r \sqrt{1 + \left(\frac{du_z}{dr}\right)^2} dr - \pi b^2 \right), \quad (A4)$$

where the limit $b \rightarrow \infty$ is taken to satisfy the above consideration of a semi-infinite medium. The Eq. (A4) depends only on d_i and R_i , since $a_c^2 = R_id_i$. We show in the Fig. 16 the values of ΔA , normalized by πd_i^2 , over a large parameter space. The integral in Eq. (A4) is numerically integrated in Python calling routines from the FORTRAN library QUADPACK.⁵³

The experimental observations made in Fig. 15 suggest that fitting Eq. (A2) to the downward deformations of the agarose hydrogels yields minimum ratios R_i/d_i that hardly fall below $R_i/d_i \approx 8$. Therefore, in a conservative estimate, we assume that the fit to the maximum hydrogel deformations is bounded at $R_i/d_i = 4$. In this case, the change in surface area over the entire parameter space of our experiments can be approximated as follows:

$$\Delta A \approx 0.4\pi d_i^2 = \frac{2}{5}\pi d_i^2. \quad (A5)$$

It follows that the potential energy stored in the stretched surface is given by

$$U_\sigma = \frac{2}{5}\pi d_i^2 \sigma. \quad (A6)$$

Imposing $U_\sigma = U_E$ finally yields the relationship between Young's modulus of the agarose hydrogels and the hypothetical surface tension

$$\sigma = \frac{4}{3\pi} \frac{ER_{max}}{(1 - \nu^2)}. \quad (A7)$$

In dimensionless form with $\bar{\sigma} = \sigma/(R_{max}\Delta p)$

$$\bar{\sigma} = \frac{4}{3\pi} \frac{E}{(1 - \nu^2)\Delta p}. \quad (A8)$$

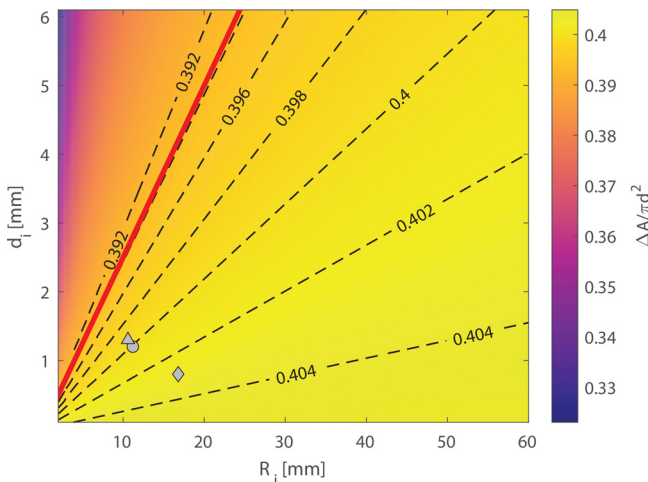


FIG. 16. Solution of integral A4, normalized by πd_i^2 , over the space of parameter d_i and R_i relevant to the present work. The solid line (red solid line) refers to the limit $R_i = 4d_i$. The marker (gray filled diamond) refers to the deformations parameters (R_i, d_i) caused by a bubble near the 1% (w/w) agarose hydrogel at $\gamma \approx 0.84$ (gray filled circle), while corresponds to the parameters associated with a bubble at $\gamma \approx 0.48$, and the gray filled triangle to a bubble at $\gamma \approx 0.35$.

APPENDIX B: MICROJET VELOCITY UNCERTAINTY ESTIMATION

Given the limited temporal and spatial resolution of the high-speed visualizations, the microjet velocity assessment presented in Sec. III may be subject to some uncertainty. Temporal uncertainties

are taken into account because the events characterizing the onset of the microjet or the piercing of the opposite bubble wall typically occur within the interframe that precedes their observation. We therefore assume a total uncertainty on the timing of these events equal the interframe time ($0.1 \mu\text{s}$ for $10 \times 10^6 \text{ frames s}^{-1}$ recording). This results in a maximum error of 6.5% on the velocity estimate. Alternatively, spatial uncertainties arise primarily in the evaluation of the spray front. The spray appears as an aggregate of microdroplets, so the determination of its front can be subjective. To account for this, we assume an error of ± 3 pixels with respect to the actual position of the spray front. This results in a maximum uncertainty of approximately $\pm 15\%$ for the smallest bubbles analyzed, i.e., a bubble collapsing at $\gamma \approx 1$ near the 2% (w/w) agarose hydrogel.

REFERENCES

- ¹E. Stride and C. Coussios, "Nucleation, mapping and control of cavitation for drug delivery," *Nat. Rev. Phys.* **1**, 495–509 (2019).
- ²K. Kooiman, S. Roovers, S. A. Langeveld, R. T. Kleven, H. Dewitte, M. A. O'Reilly, J.-M. Escoffre, A. Bouakaz, M. D. Verweij, K. Hynynen *et al.*, "Ultrasound-responsive cavitation nuclei for therapy and drug delivery," *Ultrasound Med. Biol.* **46**, 1296–1325 (2020).
- ³R. Sanwal, K. Joshi, M. Ditmans, S. S. Tsai, and W. L. Lee, "Ultrasound and microbubbles for targeted drug delivery to the lung endothelium in ARDS: Cellular mechanisms and therapeutic opportunities," *Biomedicine* **9**, 803 (2021).
- ⁴G. Mauri, L. Nicosia, Z. Xu, S. Di Pietro, L. Monfardini, G. Bonomo, G. M. Varano, F. Prada, P. D. Vigna, and F. Orsi, "Focused ultrasound: Tumour ablation and its potential to enhance immunological therapy to cancer," *Br. J. Radiol.* **91**, 20170641 (2018).
- ⁵K. B. Bader, E. Vlasisavljevich, and A. D. Maxwell, "For whom the bubble grows: Physical principles of bubble nucleation and dynamics in histotripsy ultrasound therapy," *Ultrasound Med. Biol.* **45**, 1056–1080 (2019).
- ⁶D. R. Mittelstein, J. Ye, E. F. Schibber, A. Roychoudhury, L. T. Martinez, M. H. Fekrazad, M. Ortiz, P. P. Lee, M. G. Shapiro, and M. Gharib, "Selective ablation of cancer cells with low intensity pulsed ultrasound," *Appl. Phys. Lett.* **116**, 013701 (2020).
- ⁷K. S. Mehta, J. J. Lee, A. A. Taha, E. Avgerinos, and R. A. Chaer, "Vascular applications of contrast-enhanced ultrasound imaging," *J. Vasc. Surg.* **66**, 266–274 (2017).
- ⁸M. Versluis, E. Stride, G. Lajoie, B. Dollet, and T. Segers, "Ultrasound contrast agent modeling: A review," *Ultrasound Med. Biol.* **46**, 2117–2144 (2020).
- ⁹H. Yusefi and B. Helfield, "The influence of inter-bubble spacing on the resonance response of ultrasound contrast agent microbubbles," *Ultrason. Sonochem.* **90**, 106191 (2022).
- ¹⁰T. Asshauer, C. Latz, A. Mirshahi, and C. Rathjen, "Femtosecond lasers for eye surgery applications: Historical overview and modern low pulse energy concepts," *Adv. Opt. Technol.* **10**, 393–408 (2021).
- ¹¹D. S. Ho, D. Scialabba, R. S. Terry, X. Ma, J. Chen, G. N. Sankin, G. Xiang, R. Qi, G. M. Preminger, M. E. Lipkin *et al.*, "The role of cavitation in energy delivery and stone damage during laser lithotripsy," *J. Endourol.* **35**, 860–870 (2021).
- ¹²L. Golino, G. Caiazzo, P. Calabrò, A. Colombo, M. Contarini, F. Fedele, G. Gabrielli, A. Galassi, P. Golino, F. S. di Uccio *et al.*, "Excimer laser technology in percutaneous coronary interventions: Cardiovascular laser society's position paper," *Int. J. Cardiol.* **350**, 19–26 (2022).
- ¹³T. Kodama and Y. Tomita, "Cavitation bubble behavior and bubble–shock wave interaction near a gelatin surface as a study of in vivo bubble dynamics," *Appl. Phys. B* **70**, 139–149 (2000).
- ¹⁴E.-A. Brujan, K. Nahen, P. Schmidt, and A. Vogel, "Dynamics of laser-induced cavitation bubbles near an elastic boundary," *J. Fluid Mech.* **433**, 251–281 (2001).
- ¹⁵E.-A. Brujan, K. Nahen, P. Schmidt, and A. Vogel, "Dynamics of laser-induced cavitation bubbles near elastic boundaries: Influence of the elastic modulus," *J. Fluid Mech.* **433**, 283–314 (2001).
- ¹⁶S. Gong, B. Goh, S.-W. Ohl, and B. C. Khoo, "Interaction of a spark-generated bubble with a rubber beam: Numerical and experimental study," *Phys. Rev. E* **86**, 026307 (2012).
- ¹⁷W. Xu, Y. Zhai, J. Luo, Q. Zhang, and J. Li, "Experimental study of the influence of flexible boundaries with different elastic moduli on cavitation bubbles," *Exp. Therm. Fluid Sci.* **109**, 109897 (2019).
- ¹⁸Y. Zhai, W. Xu, J. Luo, and J. Li, "Experimental study on the characteristics of microjets and shock waves of cavitation bubbles near elastic boundaries," *Ocean Eng.* **257**, 111664 (2022).
- ¹⁹S. Shaw, Y. Jin, T. Gentry, and D. Emmony, "Experimental observations of the interaction of a laser generated cavitation bubble with a flexible membrane," *Phys. Fluids* **11**, 2437–2439 (1999).
- ²⁰U. Orthaber, R. Petkovšek, J. Schille, L. Hartwig, G. Hawlina, B. Drnovšek-Olup, A. Vrečko, and I. Poberaj, "Effect of laser-induced cavitation bubble on a thin elastic membrane," *Opt. Laser Technol.* **64**, 94–100 (2014).
- ²¹A. H. Aghdam, S. Ohl, B. Khoo, M. Shervani-Tabar, and M. Nobari, "Effect of the viscosity on the behavior of a single bubble near a membrane," *Int. J. Multiphase Flow* **47**, 17–24 (2012).
- ²²Ž. Lokar, R. Petkovšek, and M. Dular, "Cavitation bubble dynamics in a vicinity of a thin membrane wetted by different fluids," *Sci. Rep.* **11**, 3506 (2021).
- ²³E. Klaseboer and B. C. Khoo, "Boundary integral equations as applied to an oscillating bubble near a fluid-fluid interface," *Comput. Mech.* **33**, 129–138 (2004).
- ²⁴E. Klaseboer and B. C. Khoo, "An oscillating bubble near an elastic material," *J. Appl. Phys.* **96**, 5808–5818 (2004).
- ²⁵C. K. Turangan, G. P. Ong, E. Klaseboer, and B. C. Khoo, "Experimental and numerical study of transient bubble-elastic membrane interaction," *J. Appl. Phys.* **100**, 054910 (2006).
- ²⁶S. W. Fong, E. Klaseboer, C. K. Turangan, B. C. Khoo, and K. C. Hung, "Numerical analysis of a gas bubble near bio-materials in an ultrasound field," *Ultrasound Med. Biol.* **32**, 925–942 (2006).
- ²⁷G. A. Curtiss, D. M. Leppinen, Q. X. Wang, and J. R. Blake, "Ultrasonic cavitation near a tissue layer," *J. Fluid Mech.* **730**, 245–272 (2013).
- ²⁸S. Wang, Q. Wang, D. Leppinen, A. Zhang, and Y. Liu, "Acoustic bubble dynamics in a microvessel surrounded by elastic material," *Phys. Fluids* **30**, 012104 (2018).
- ²⁹A. B. Mathur, A. M. Collinworth, W. M. Reichert, W. E. Kraus, and G. A. Truskey, "Endothelial, cardiac muscle and skeletal muscle exhibit different viscous and elastic properties as determined by atomic force microscopy," *J. Biomech.* **34**, 1545–1553 (2001).
- ³⁰K. E. Hamilton and D. C. Pye, "Young's modulus in normal corneas and the effect on applanation tonometry," *Optom. Vis. Sci.* **85**, 445–450 (2008).
- ³¹N. F. Davis, J. J. Mulvihill, S. Mulay, E. M. Cunnane, D. M. Bolton, and M. T. Walsh, "Urinary bladder vs gastrointestinal tissue: A comparative study of their biomechanical properties for urinary tract reconstruction," *Urology* **113**, 235–240 (2018).
- ³²V. Normand, D. L. Lootens, E. Amici, K. P. Plucknett, and P. Aymard, "New insight into agarose gel mechanical properties," *Biomacromolecules* **1**, 730–738 (2000).
- ³³K. Upadhyay, G. Subhash, and D. Spearot, "Hyperelastic constitutive modeling of hydrogels based on primary deformation modes and validation under 3D stress states," *Int. J. Eng. Sci.* **154**, 103314 (2020).
- ³⁴A. Ed-Daoui and P. Snabre, "Poroviscoelasticity and compression-softening of agarose hydrogels," *Rheol. Acta* **60**, 327–351 (2021).
- ³⁵A. Sieber, D. Preso, and M. Farhat, "Dynamics of cavitation bubbles near granular boundaries," *J. Fluid Mech.* **947**, A39 (2022).
- ³⁶W. Lauterborn, C. Lechner, M. Koch, and R. Mettin, "Bubble models and real bubbles: Rayleigh and energy-deposit cases in a Tait-compressible liquid," *IMA J. Appl. Math.* **83**, 556–589 (2018).
- ³⁷C. Lechner, W. Lauterborn, M. Koch, and R. Mettin, "Fast, thin jets from bubbles expanding and collapsing in extreme vicinity to a solid boundary: A numerical study," *Phys. Rev. Fluids* **4**, 021601 (2019).
- ³⁸J. R. Blake, B. B. Taib, and G. Doherty, "Transient cavities near boundaries. Part 1. Rigid boundary," *J. Fluid Mech.* **170**, 479–497 (1986).
- ³⁹O. Supponen, D. Obreschkow, M. Tinguely, P. Kobel, N. Dorsaz, and M. Farhat, "Scaling laws for jets of single cavitation bubbles," *J. Fluid Mech.* **802**, 263–293 (2016).

- ⁴⁰G. Subhash, Q. Liu, D. Moore, P. Ifju, and M. Haile, “Concentration dependence of tensile behavior in agarose gel using digital image correlation,” *Exp. Mech.* **51**, 255–262 (2011).
- ⁴¹C. Lechner, W. Lauterborn, M. Koch, and R. Mettin, “Jet formation from bubbles near a solid boundary in a compressible liquid: Numerical study of distance dependence,” *Phys. Rev. Fluids* **5**, 093604 (2020).
- ⁴²Y. A. Pishchalnikov, W. M. Behnke-Parks, K. Schmidmayer, K. Maeda, T. Colonius, T. W. Kenny, and D. J. Laser, “High-speed video microscopy and numerical modeling of bubble dynamics near a surface of urinary stone,” *J. Acoust. Soc. Am.* **146**, 516–531 (2019).
- ⁴³F. Reuter and C.-D. Ohl, “Supersonic needle-jet generation with single cavitation bubbles,” *Appl. Phys. Lett.* **118**, 134103 (2021).
- ⁴⁴S. P. Lin and R. D. Reitz, “Drop and spray formation from a liquid jet,” *Annu. Rev. Fluid Mech.* **30**, 85 (1998).
- ⁴⁵T. Alghamdi, S. T. Thoroddsen, and J. F. Hernández-Sánchez, “Ultra-high speed visualization of a flash-boiling jet in a low-pressure environment,” *Int. J. Multiphase Flow* **110**, 238–255 (2019).
- ⁴⁶W. V. Kayser, “Temperature dependence of the surface tension of water in contact with its saturated vapor,” *J. Colloid Interface Sci.* **56**, 622–627 (1976).
- ⁴⁷C.-D. Ohl and S.-W. Ohl, “Shock wave interaction with single bubbles and bubble clouds,” in *Bubble Dynamics and Shock Waves* (Springer, 2013), pp. 3–31.
- ⁴⁸K. Tang, W. Mostert, D. Fuster, and L. Deike, “Effects of surface tension on the Richtmyer-Meshkov instability in fully compressible and inviscid fluids,” *Phys. Rev. Fluids* **6**, 113901 (2021).
- ⁴⁹M. Brouillette, “The Richtmyer-Meshkov instability,” *Annu. Rev. Fluid Mech.* **34**, 445 (2002).
- ⁵⁰V. L. Popov, *Contact Mechanics and Friction* (Springer, 2010).
- ⁵¹H. Hertz, “Über die berührung fester elastischer körper,” *J. Reine Angew. Math.* **1882**, 156–171.
- ⁵²V. L. Popov, M. Heß, and E. Willert, *Handbook of Contact Mechanics: Exact Solutions of Axisymmetric Contact Problems* (Springer Nature, 2019).
- ⁵³R. Piessens, E. de Doncker-Kapenga, C. W. Überhuber, and D. K. Kahaner, *Quadpack: A Subroutine Package for Automatic Integration* (Springer Science & Business Media, 2012), Vol. 1.